

Toward atomic resolution diffractive imaging of isolated molecules with x-ray free-electron lasers

Stephan Stern,^{ab} Lotte Holmegaard,^{ae} Frank Filsinger,^{fg,1} Arnaud Rouzée,^{hi} Artem Rudenko,^{gjk} Per Johnsson,^l Andrew V. Martin,^{a,2} Anton Barty,^a Christoph Bostedt,^m John Bozek,^m Ryan Coffee,^m Sascha Epp,^{gj} Benjamin Erk,^{cgj} Lutz Foucar,^{gn} Robert Hartmann,^o Nils Kimmel,^p Kai-Uwe Kühnel,^j Jochen Maurer,^e Marc Messerschmidt,^m Benedikt Rudek,^{gj,3} Dmitri Starodub,^{q,4} Jan Thøgersen,^e Georg Weidenspointner,^{pr,5} Thomas A. White,^a Henrik Stapelfeldt,^{es} Daniel Rolles,^{cgn} Henry N. Chapman,^{abc} and Jochen Küpper^{abc*}

Received Xth XXXXXXXXXXXX 2014,

Accepted Xth XXXXXXXXXXXX 2014

First published on the web Xth XXXXXXXXXXXX 2014

DOI: 10.1039/c0xxxxx

We give a detailed account of the theoretical analysis and the experimental results of an x-ray-diffraction experiment on quantum-state selected and strongly laser-aligned gas-phase ensembles of the prototypical large asymmetric rotor molecule 2,5-diiodobenzonitrile, performed at the Linac Coherent Light Source [*Phys. Rev. Lett.* **112**, 083002 (2014)]. This experiment is the first step toward coherent diffractive imaging of structures and structural dynamics of isolated molecules at atomic resolution, i. e., picometers and femtoseconds, using x-ray free-electron lasers.

^a Center for Free-Electron Laser Science (CFEL), Deutsches Elektronen-Synchrotron (DESY), Notkestrasse 85, 22607 Hamburg, Germany.

E-mail: jochen.kuepper@cfel.de, URL: <http://desy.cfel.de/cid/cmi>

^b Department of Physics, University of Hamburg, Luruper Chaussee 149, 22761 Hamburg, Germany.

^c Deutsches Elektronen-Synchrotron (DESY), Notkestrasse 85, 22607 Hamburg, Germany.

^d The Hamburg Center for Ultrafast Imaging, University of Hamburg, Luruper Chaussee 149, 22761 Hamburg, Germany.

^e Aarhus University, Department of Chemistry, 8000 Aarhus C, Denmark.

^f Fritz Haber Institute of the MPG, Faradayweg 4–6, 14195 Berlin, Germany.

^g Max Planck Advanced Study Group at CFEL, Notkestrasse 85, 22607 Hamburg, Germany.

^h FOM Institute AMOLF, Science Park 104, 1098 XG Amsterdam, The Netherlands.

ⁱ Max-Born-Institute, Max Born Str. 2a, 12489 Berlin, Germany.

^j Max Planck Institute for Nuclear Physics, 69117 Heidelberg, Germany.

^k J. R. Macdonald Laboratory, Department of Physics, Kansas State University, Manhattan, KS 66506, USA.

^l Lund University, Department of Physics, P. O. Box 118, 22100 Lund, Sweden.

^m Linac Coherent Light Source, SLAC National Accelerator Laboratory, 2575 Sand Hill Road, Menlo Park, CA 94025, USA.

ⁿ Max Planck Institute for Medical Research, 69120 Heidelberg, Germany.

^o PNSensor GmbH, 81739 Munich, Germany.

^p Max Planck Semiconductor Laboratory, 81739 Munich, Germany.

^q Department of Physics, Arizona State University, Tempe, AZ 85287, USA.

^r Max Planck Institute for Extraterrestrial Physics, 85741 Garching, Germany.

^s Aarhus University, Interdisciplinary Nanoscience Center (iNANO), 8000 Aarhus C, Denmark.

1 Introduction

The advent of X-ray Free-Electron Lasers (XFELs) opens up new and previously inaccessible research directions in physical and chemical sciences. One of the major scopes is the utilization of XFEL radiation in diffractive imaging experiments. Collecting single-shot x-ray diffraction patterns with the ultrashort, currently down to a few femtoseconds, x-ray pulses of extremely high brilliance at an XFEL allows the conventional damage limit in imaging of non-crystalline biological samples to be circumvented.¹ Experiments at the Linac Coherent Light Source (LCLS) confirmed the feasibility of utilizing XFELs for femtosecond single-shot imaging of non-crystalline biological specimens² as well as for femtosecond nanocrystallography of proteins.³

These results provide important steps on the path towards the paramount goal of atomically (picometer and femtoseconds) resolved diffractive imaging of structures and ultrafast structural dynamics during chemical reactions of even single molecules. However, the path toward this goal, often nicknamed as “recording of a molecular movie”, is still long and many challenges have to be overcome in order to achieve the required spatio-temporal resolution.^{4,5} The usually proposed experimental approach is to provide identical molecules, delivered in a liquid or gaseous stream to the focus of an XFEL.^{6,7} Since the high single-shot XFEL intensity by far exceeds the damage threshold of single molecules, the molecules have to be replenished in each shot. Single-molecule diffraction data has to be collected for many shots with the molecule at many different orientations in order to fill up the three-dimensional diffraction volume. The relative orientation of single-molecule diffraction patterns from distinct shots could be determined computationally from the diffraction patterns themselves provided that the single-molecule diffraction signal is well above noise.^{8–10} However, one of the main issues in single-molecule x-ray diffraction experiments is the weak scattering signal from single molecules, which, so far, is too weak to allow for orientation classification solely from the diffraction pattern, even at the high intensities of the novel XFELs. Therefore, diffraction data has to be recorded and averaged for many shots with the molecule at the same, pre-imposed alignment and/or orientation * in space in order to obtain an interpretable diffraction pattern above noise. Strong molecular alignment in the laboratory frame can be achieved, for instance, through adiabatic laser alignment, while orientation requires additional dc electric fields.^{11–14} Alignment and orientation can be varied easily by controlling the the alignment laser polarization and, in case orientation is utilized as well, the direction of the dc field. Utilizing ensembles of such aligned molecules allows for averaging of many identical patterns, similar to recent experiments exploiting electron diffraction from CF₃I [15] or photoelectron imaging of 1-ethynyl-4-fluorobenzene^{16,17} and dibromobenzene.¹⁸

An obstacle to this concept is that complex large molecules typically exist in various structural isomers, e. g., conformers, which are often difficult to separate due to the small energy difference and low barriers between them. However, to achieve atomic-resolution in diffractive imaging experiments they have to be analyzed separately. We have proposed⁷ to solve this by spatially separating

* Alignment refers to fixing one or more molecular axes in space, while orientation refers to breaking of the corresponding up-down symmetry.

shapes,¹⁹ sizes,²⁰ or individual isomers^{21–23} of the molecules before delivery to the interaction point of the experiment. These pre-selected ensembles can be efficiently, one- and three-dimensionally, aligned or oriented in the laboratory frame.^{13,24,25}

Here, we give a detailed account of an x-ray diffraction experiment of ensembles of isolated gas-phase molecules at the Linac Coherent Light Source (LCLS).²⁶ Cold, state-selected, and aligned ensembles of the prototypical molecule 2,5-diiodobenzonitrile (C₇H₃I₂N, DIBN) were irradiated with XFEL pulses with a photon energy of 2 keV ($\lambda = 620$ pm) and x-ray diffraction data was recorded and analyzed. DIBN was utilized for this proof-of-principle experiment because it contains two heavy atoms (iodine) and it can be laser-aligned along an axis almost exactly coinciding with the iodine-iodine axis. Therefore, as the two-center iodine-iodine interference dominates the scattering signal, the experiment resembles Young's double slit on the atomic level. We achieved strong laser-alignment of the ensemble of DIBN molecules which allowed for averaging of many patterns from these weakly scattering molecules.

The outline of this paper is as follows: In section 2 the experimental setup is introduced. This includes details on the preparation of the molecular sample for the x-ray diffraction experiment: we present measurements of the molecular beam deflection profiles and two-dimensional ion-momentum distributions from which the molecular alignment of DIBN is quantified. In addition, the process of data acquisition, background subtraction, and spatial single-photon counting with the pnCCD photon detector^{27,28} is outlined very briefly, while a comprehensive explanation of all the steps involved in the procedure of conditioning and correcting the x-ray diffraction data is given in Appendix A. The theory behind the numerical simulations of x-ray diffraction intensities to be compared with the experimental diffraction data is outlined in section 3. In section 4 the experimental results are presented and the manuscript concludes with a summary of the experimental findings and an outlook on future experiments in section 5.

2 Experimental

2.1 Experimental setup

The experiment was performed at the Atomic, Molecular, and Optical Physics (AMO) beamline^{29,30} of LCLS,³¹ using the CAMP (CFEL-ASG Multi-Purpose) experimental chamber.^{27,32} The CAMP instrument was equipped with a state-of-the-art molecular beam setup providing gas-phase ensembles of cold and quantum-state selected target molecules.^{20–24} For the x-ray diffraction experiment, a photon energy of 2 keV ($\lambda = 620$ pm) was used, which is the maximum photon energy available at AMO. The 2 keV x-ray pulses were focussed by a Kirkpatrick-Baez (KB) mirror system into the CAMP experimental chamber, which was attached to the High Field Physics (HFP) chamber at the AMO beamline. The CAMP instrument contains multiple detectors to detect photons, electrons, and ions simultaneously and it is described in detail elsewhere.²⁷

Figure 1 shows a schematic view of the experimental setup inside CAMP. During the experiment, a pulsed molecular beam was formed by a supersonic expansion of a mixture of a few mbar of DIBN and 50 bar of helium (He) into

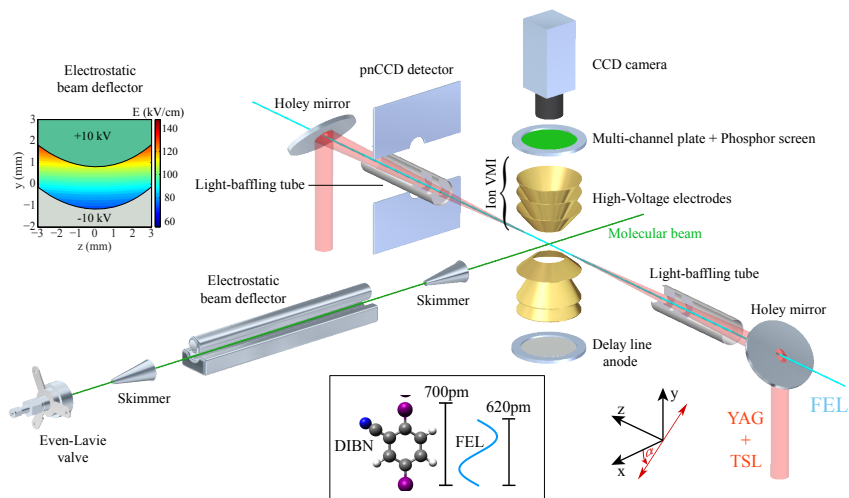


Fig. 1 Schematic view of the experimental setup inside the CAMP experimental chamber. The molecular beam, created by supersonic expansion of DIBN and He from the Even-Lavie valve on the left, enters the deflector and quantum-state selected molecules are delivered to the interaction point. In the center of the velocity map imaging spectrometer (VMI) the molecular beam is crossed by the laser beams copropagating from right to left. The direct laser beams pass through a gap in the pnCCD photon detectors that are used to record the x-ray diffraction pattern. The upper pnCCD panel is further away from the beam axis than the bottom panel in order to cover a wider range of scattering angles. The inlet on the upper left shows a cross section of the electrostatic beam deflector along the propagation direction of the molecular beam. The inlet on the lower edge illustrates the two significant lengthscales of the x-ray diffraction experiment, namely the molecular structure of DIBN with the iodine-iodine distance and the x-ray wavelength. The molecular structure of DIBN was obtained from *ab initio* calculations (GAMESS-US,³³ MP2/6-311G**), which predict a value of 700 pm for the iodine-iodine distance. Figure reproduced from ref. 26.

vacuum through an Even-Lavie valve.³⁴ The target molecules were cooled to low rotational temperatures of ~ 1 K in the early stage of the expansion by collisions with the He seed gas.^{35,36} Traveling through the electrostatic deflector, the molecules were dispersed along the vertical (y) axis according to their effective dipole moment, i. e., their quantum state. The deflector consists of two 24 cm-long electrodes, a cylindrical rod electrode at the top and a trough electrode at the bottom. The vertical distance between the two electrodes in the horizontal center of the deflector is 2.3 mm. By application of high static electric potentials of ± 10 kV to the top and bottom electrodes, a strong inhomogeneous static electric field was created with an electric field strength of 120 kV/cm and an electric field gradient of 250 kV/cm² in the center of the deflector as depicted in the inlet of Figure 1. Quantum-state selection via the deflector is achieved due to the different Stark effect of distinct quantum states (*vide infra*). Furthermore, spatial separation of polar DIBN and non-polar He seed gas in the deflector was utilized to reduce the scattering background from the He in the x-ray diffraction experiment.

After passing through the deflector, the quantum-state dispersed molecular beam entered the detection chamber where it was crossed by three pulsed laser beams: Pulses from a Nd:YAG laser (YAG, 12 ns (FWHM), $\lambda = 1064$ nm, $E_I = 200$ mJ, $\omega_0 = 63$ μm , $I_0 \approx 2.5 \cdot 10^{11}$ W/cm²) were used to align the ensemble of target molecules. The second laser, a Ti:Sapphire laser (TSL, 60 fs (FWHM), 800 nm, $E_I = 400$ μJ , $\omega_0 = 40$ μm , $I_0 \approx 2.5 \cdot 10^{14}$ W/cm²) was used to ionize DIBN in order to optimize the molecular beam and the alignment without the LCLS beam. X-ray pulses from LCLS (100 fs, estimated from electron bunch length and pulse duration measurements,³⁷ $\lambda = 620$ pm, $E_I = 4$ mJ, $\omega = 30$ μm , $I_0 \approx 2 \cdot 10^{15}$ W/cm²) were used to probe the ensemble of aligned DIBN. We deliberately worked out-of-focus of the x-ray beam at low fluence in order to mitigate electronic^{38–40} and nuclear damage processes.⁴¹ The x-ray photons diffracted from the ensemble were collected by the pnCCD photon detector at a distance (i. e., camera length) of 71 mm. 35% of the generated $1.25 \cdot 10^{13}$ x-ray photons/pulse were estimated to be transported to the experiment.⁴² The two panels of the pnCCD detector were opened by a significant amount in order to cover large scattering angles, i. e., the top pnCCD panel was moved by 44 mm (covering scattering angles of $31^\circ \leq 2\Theta \leq 50^\circ$) and the bottom panel to a distance of 17 mm ($13^\circ \leq 2\Theta \leq 38^\circ$) from the z -axis. All three laser beams were co-propagating, overlapped using dichroic (1064 nm and 800 nm) and holey (x-ray and infrared beams) mirrors. After intersecting the sample the lasers finally left the setup through a gap between the two panels of the pnCCD camera and another holey mirror in the back of the CAMP chamber to separate the laser beams again. Straylight from the optical lasers was reduced using a set of apertures mounted in a small tube directly in front of the interaction zone (named “light baffling tube” in Figure 1). A similar light baffling tube was mounted downstream the interaction zone, reaching between the two pnCCD panels and containing a similar set of apertures in order to suppress straylight from optical or x-ray photons impinging from the back of the CAMP chamber onto the back of the pnCCD panels. In addition, the front side (i. e., the side facing the interaction zone) of each pnCCD panel was covered using aluminum-coated filters in order to further suppress straylight from the optical lasers.

The CAMP chamber was equipped with a dual velocity-map-imaging (VMI) spectrometer in order to measure two-dimensional ion momentum distributions in the x - z plane, resulting from Coulomb explosion due to absorption of one or a few x-ray photons (or optical photons in case the TSL was utilized to probe the molecular alignment).²⁷ Operation of the VMI spectrometer as an ion time-of-flight (TOF) spectrometer in quasi-Wiley-McLaren configuration⁴³ allowed for mass selective detection of individual ionic fragments.

The x-ray diffraction experiment was performed with LCLS running at a repetition rate of 60 Hz while the YAG was running at 30 Hz. Hence, a dataset contains shots of aligned and randomly oriented molecules in an alternating manner. All diffraction measurements were conducted in the deflected part of the molecular beam, i. e., at (nearly) optimal molecular alignment (*vide infra*). In the following, experimental results concerning preparation of the molecular ensemble for the x-ray diffraction experiment are presented, namely quantum-state selection by deflection and laser-alignment.

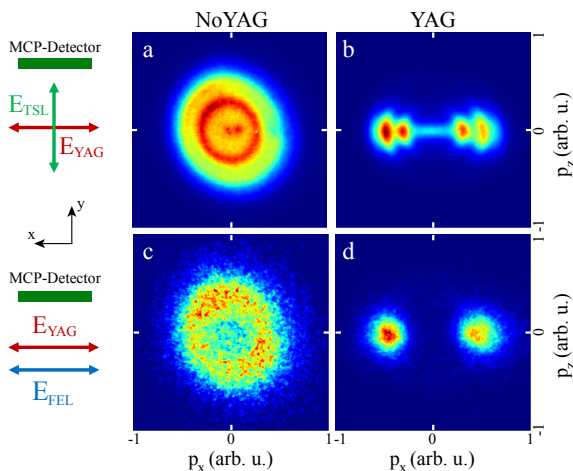


Fig. 2 I^+ ion momentum distributions recorded with the ion-VMI and MCP detector when the TSL (a,b) or the LCLS (c, d) was used to ionize and Coulomb explode the molecules. In (a, c) cylindrically symmetric distributions from isotropic ensembles are observed (the images are slightly distorted due to varying detector efficiencies). In (b, d) the horizontal alignment of the molecules, induced by the YAG, is clearly visible. In all measurements the YAG and the LCLS are linearly polarized along the x -axis, i. e., parallel to the detector plane, and the TSL is linearly polarized along the y -axis, i. e., perpendicular to the detector plane. Figure reproduced from ref. 26.

2.2 Quantum-state selection and laser alignment

The benefit of quantum-state selection prior to laser alignment for cold ensembles of asymmetric top molecules¹³ was exploited in our experiment in order to obtain strong alignment of the molecular sample for the x -ray diffraction experiment. For a large asymmetric top molecule such as DIBN, all populated rotational states in the molecular beam are so-called high-field-seeking (hfs) states. Molecules in these states are deflected towards increasing electric field strength, i. e., upwards along the y -axis.^{24,44} The lowest states typically exhibit the largest Stark energy shift and, thus, the strongest deflection. Quantum-state selection is very beneficial for laser-alignment: As the lowest-lying states experience a stronger angular confinement in the electric field of a linearly polarized alignment laser, selection of the lowest-lying states prior to alignment significantly improves the degree of alignment.^{13,24,25}

When the linearly polarized YAG was included, DIBN molecules aligned along their most-polarizable axis, which is nearly coincident with the iodine-iodine (I–I) axis. Utilizing Coulomb explosion imaging of aligned DIBN, induced by either the TSL or the FEL, strong alignment of DIBN ensembles was confirmed by two-dimensional momentum distributions of I^+ ions (which recoil along the iodine-iodine axis) recorded with the velocity-map imaging (VMI) spectrometer. Figure 2 shows corresponding I^+ momentum distributions, recorded with (YAG) and without (NoYAG) the YAG alignment laser. In the NoYAG case, the I^+ images are circularly symmetric corresponding to an ensemble of isotropically-distributed molecules. The circularly symmetric image

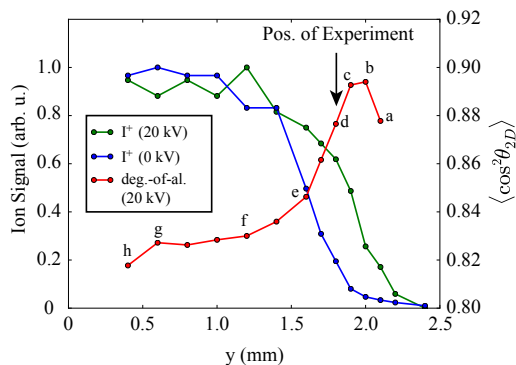


Fig. 3 The molecular beam density profiles, obtained by recording the I^+ signal (see left vertical axis) at different positions along the y -axis in the molecular beam for the undeflected (blue) and deflected (green) molecular beam. The different degree of alignment of DIBN in terms of $\langle \cos^2 \theta_{2D} \rangle$ (right vertical axis) at different positions in the deflected molecular beam illustrates the dispersion of quantum states (red). Considering the best compromise between degree of alignment and sufficient molecular beam density of target molecules, the x-ray diffraction experiment was performed at $y = 1.8$ mm ($\langle \cos^2 \theta_{2D} \rangle = 0.877$), not at the position where the highest degree of alignment was observed, i. e., $\langle \cos^2 \theta_{2D} \rangle = 0.894$ at $y = 2$ mm.

Figure 2 c, obtained following ionization with the horizontally polarized FEL also demonstrated that the interaction of the far-off resonant radiation with the molecule was independent of the angle between the molecular axis and the x-ray polarization direction: The x rays were a practically unbiased ideal probe of spatial orientation of molecules. Including the YAG laser, I^+ ions were strongly confined along the polarization axis of the YAG. The two distinct pairs of peaks in the TSL case correspond to two distinct ionization channels yielding I^+ ions from doubly and triply ionized molecules.⁴⁵ The degree of alignment is quantified by calculating $\langle \cos^2 \theta_{2D} \rangle$, where θ_{2D} is the angle with respect to the laser polarization axis in the projected, two-dimensional I^+ momentum distributions.

The deflector was utilized to improve the degree of alignment by quantum-state selection of the lowest states. Figure 3 shows molecular beam density profiles obtained by measuring the I^+ signal probed at distinct positions along the y -axis when the deflector was off (blue) or on (green, 20 kV). Both graphs were normalized to the peak intensity. Only the upper part of the molecular beam was probed. The different deflection of distinct quantum states in the molecular beam leads to a shift of the beam profile as is shown in Figure 3. The corresponding dispersion of quantum states can be illustrated by recording I^+ momentum distributions at distinct positions: as expected, the degree of alignment is significantly enhanced in the deflected part of the molecular beam. The resulting $\langle \cos^2 \theta_{2D} \rangle$ values are depicted by the red graph of Figure 3 and the enhanced alignment in the deflected part of the molecular beam is obvious. The strongest alignment, quantified by $\langle \cos^2 \theta_{2D} \rangle = 0.894$, was obtained at $y = 2$ mm. However, to utilize a higher beam density, the x-ray diffraction experiment was performed at $y = 1.8$ mm. At this position the degree of alignment was only slightly smaller ($\langle \cos^2 \theta_{2D} \rangle = 0.877$), but the molecular beam density was still 60 % of the unde-

flected beam density, whereas it was only 20 % at $y = 2$ mm.

During the x-ray diffraction experiment, the YAG polarization was rotated to $\alpha = -60^\circ$ with respect to the horizontal axis. The alignment was probed repeatedly over the course of the x-ray diffraction measurement period of ~ 8 h and the average degree of alignment was $\langle \cos^2 \theta_{2D} \rangle = 0.84$, mainly due to variations of the overlap of the YAG and FEL pulses. The degree of alignment is in agreement with measurements of adiabatic alignment of quantum-state selected ensembles of similar molecules^{13,25} and matches requirements for diffraction experiments on aligned molecules.^{7,15}

2.3 X-ray diffraction data acquisition

A comprehensive description of the data conditioning procedure is given in Appendix A. In summary, single shot x-ray diffraction data was recorded by the pnCCD detectors and saved to file. Several sources of background signals (offset, gain, experimental background from the YAG alignment laser, etc.) and detector artifacts (“hot-pixels”, etc.) were subtracted from the data by utilizing the CFEL-ASG Software Suite (CASS).³² Eventually, single x-ray photon hits were extracted by application of a 3σ -threshold to these “clean” single-shot pnCCD data frames. This procedure yields 0.2 x-ray photons per shot (i. e., on average only one scattered x-ray photon in five shots) that are scattered to the pnCCD detector. These photons are placed in a histogram which represents the molecular diffraction pattern obtained from aligned (labelled “YAG”) and isotropically distributed (“NoYAG”) ensembles of DIBN molecules.

3 Simulation of x-ray diffraction intensities

Diffraction intensities from ensembles of aligned and not-aligned DIBN molecules and the He seed gas were simulated for comparison with the experimental data. Unless stated otherwise, the underlying theory is either explicitly given by the book of Als-Nielsen & McMorrow⁴⁶ or was derived from there.⁴⁷

X-ray scattering off ensembles of isolated molecules is very weak and hence the kinematical approximation (first Born approximation) is assumed to be valid, meaning that multiple scattering of a single photon is highly unlikely and can be neglected. For all calculations, the interaction point is regarded as the origin of the coordinate system. Then, the number of x-ray photons I_{sc} that are scattered from a single molecule to a certain pixel at position \mathbf{R} can be calculated as

$$I_{sc} = \left[r_0 \cdot F_{\text{mol}}(\mathbf{q}) \cdot e^{i\mathbf{k}\mathbf{R}} \right]^2 \cdot \Delta\Omega \cdot P \cdot \frac{I_0}{A_0} \quad (1)$$

where r_0 is the Thomson scattering length of the electron which is given by

$$r_0 = \frac{e^2}{4\pi\epsilon_0 mc^2} = 2.82 \cdot 10^{-5} \text{ \AA} \quad (2)$$

Utilizing conventional notation, $\mathbf{q} = \mathbf{k} - \mathbf{k}'$ is the scattering vector with \mathbf{k} and \mathbf{k}' being the wavevectors of the incident and scattered waves, respectively. $F_{\text{mol}}(\mathbf{q})$ is the molecular scattering factor (see below). $\Delta\Omega$ is the solid angle a certain pixel

subtends to the incident XFEL beam, and P is the polarization factor depending on the x-ray source. Since LCLS is linearly polarized (along the x -axis), P takes the following form: $P(\mathbf{k}') = 1 - |\hat{\mathbf{u}} \cdot \hat{\mathbf{k}}'|^2$ with the unit vector $\hat{\mathbf{u}}$ pointing along the x -axis.⁴⁸ Finally, the number of incident photons is given by I_0 and the cross-sectional area of the incident x-ray beam is represented by A_0 .

The scattering factor of a molecule $F_{\text{mol}}(\mathbf{q})$ is modeled as the sum of the atomic scattering factors $f_j(\mathbf{q})$ of the constituent j atoms (located at the positions \mathbf{r}_j within the molecule) times the phase factor $e^{i\mathbf{q}\mathbf{r}_j}$, hence

$$F_{\text{mol}}(\mathbf{q}) = \sum_j f_j(\mathbf{q}) e^{i\mathbf{q}\mathbf{r}_j} \quad (3)$$

A model of the atomic scattering factors f_j has been given by Waasmaier & Kirfel⁴⁹ by modelling atomic scattering factors in dependence of the scattering momentum transfer $s = \sin \Theta / \lambda$ as the sum of five gaussian functions and a constant.

$$f(s) = \sum_{i=1}^5 a_i e^{-b_i s^2} + \text{const.} \quad (4)$$

For the calculations presented here, the atomic scattering factors were modified by dispersion corrections given by Henke et al.,⁵⁰ thereby accounting for the dependence of the scattering strength from the photon energy.

(1) was used to calculate the diffraction pattern for a perfectly aligned molecule. However, the experimental diffraction pattern of an ensemble of DIBN molecules with a finite (i. e., non-perfect) degree of alignment is the incoherent superposition of single-molecule diffraction patterns at slightly different orientations with respect to the (linear) laser polarisation of the YAG. The relative weight of different orientations are described by an alignment-angular distribution function giving the relative population $n(\theta)$ where θ is the angle with respect to the YAG polarisation axis. The following approximation for strong alignment was applied in our model:⁵¹

$$n(\theta) = \exp\left(-\frac{\sin^2 \theta}{2\sigma^2}\right) \quad (5)$$

In practice, the blurred single-molecule diffraction pattern was obtained by averaging of single-molecule diffraction patterns calculated for 1000 distinct orientations of DIBN, weighted by (5). Then, this pattern is multiplied by the number of molecules N in the interaction volume V_0 in order to obtain the diffraction pattern of N molecules. However, as long as the x-ray beam is smaller than the molecular beam, the absolute number doesn't have to be known but rather the number density M of molecules: The number of molecules N can be written as $N = M \cdot V_0 = M \cdot A_0 \cdot l$ where the interaction volume is approximated as a cylindrical volume of length l in z -direction, and, in our case, l is the width of the molecular beam which is ≈ 4 mm (determined by the last skimmer). Therefore, once (1) was multiplied by N , the factor N/A_0 in (1) could be replaced by $M \cdot l$.

Figure 4 shows simulated diffraction patterns, i. e., the number of scattered photons on a plane detector at a camera length of 71 mm, for different degrees of alignment for 565 000 shots ($4.375 \cdot 10^{12}$ photons/shot), and a molecular beam density of $M = 1.2 \cdot 10^8 \text{ cm}^{-3}$. The molecules were aligned at $\alpha = -60^\circ$

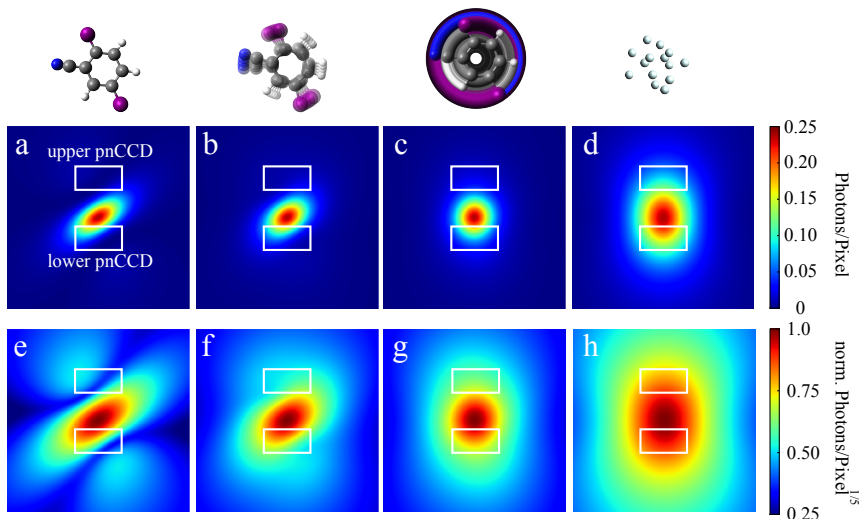


Fig. 4 Simulated scattering intensities for different degrees of alignment. a–d correspond to DIBN aligned with $\langle \cos^2 \theta_{2D} \rangle = 0.99$ (a), 0.84 (b), 0.5 (isotropic, c). The signal for 5580 He atoms (d) is the same as the DIBN signal at $\mathbf{q} = 0$. To illustrate interference features (i. e., the weak first order diffraction maxima), the second row (e–h) shows the fifth root of the normalized intensities of the first row.

with respect to the horizontal plane. White rectangles mark the position of the pnCCDs in the experiment. Images a–c correspond to DIBN aligned with $\langle \cos^2 \theta_{2D} \rangle = 0.99$ (a), 0.83 (b), 0.5 (isotropic, c). The diffraction signal from 5580 He atoms (d) at $\mathbf{q} = 0$ is equal to the diffraction signal from a single DIBN molecule at $\mathbf{q} = 0$. We do not exactly know the ratio of He atoms per DIBN molecule in our molecular beam, but it is in the 10^4 – 10^5 range. In order to illustrate interference features of the weak first order diffraction maxima, a different colorscale has been applied, enhancing the first-order iodine-iodine diffraction maxima: therefore, the second row (e–h) shows the fifth root of the normalized intensities. The main interference feature, originating in the interference of the two iodine atoms, is clearly visible for nearly perfect alignment, i. e., in Figure 4 (e) while non-perfect alignment (f) significantly washes out the interference features at high angles.

4 Results and discussion

Diffraction patterns I_{NoYAG} and I_{YAG} were constructed independently for isotropic (NoYAG) and aligned (YAG) samples, respectively, by summing all photon hits in the energy range around 2 keV, corresponding to 1500–3200 ADU (analog-to-digital unit, see Appendix A) into a two-dimensional histogram. The resulting images are shown in Figure 15 c and d in Appendix A. In addition to the diffraction signal from aligned DIBN, the I_{NoYAG} - and I_{YAG} -data contain experimental background such as the isotropic atomic scattering from all individual atoms of DIBN, scattering from the helium seed gas, scattering from residual gas in the chamber, and scattering at apertures in the laser beam path. Since the scattering

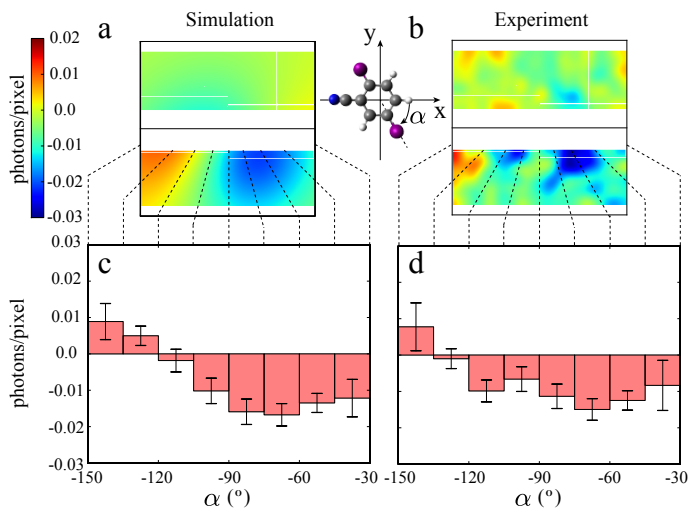


Fig. 5 Diffraction-difference $I_{\text{YAG}} - I_{\text{NoYAG}}$ of x-ray scattering in simulated (a) and experimental (b) x-ray-diffraction patterns. Histograms of the corresponding angular distributions on the bottom pnCCD (c, d) illustrate the angular anisotropy of the diffraction signal. Error bars correspond to 1σ statistical errors from Poisson noise. The molecular beam density in (a) is $M = 0.8 \cdot 10^8 \text{ cm}^{-3}$. Figure reproduced from ref. 26.

background from all these sources is the same under NoYAG and YAG conditions, it cancels out when calculating $I_{\text{YAG}} - I_{\text{NoYAG}}$.

Figure 5 shows the diffraction-difference pattern $I_{\text{YAG}} - I_{\text{NoYAG}}$ for (a) simulated and (b) experimentally recorded x-ray diffraction data. The I_{NoYAG} data has been scaled to match the number of shots of the I_{YAG} data. The difference is almost entirely due to the iodine-iodine interference which dominates the anisotropic part of the scattering signal. The most notable diffraction features are the zeroth-order maximum and the first-order minimum appearing on the bottom pnCCD panel (i. e., at low resolution). The anisotropy of the diffraction signal of aligned DIBN is illustrated by the angular anisotropy with respect to the alignment angle α as shown in Figure 5 c, d. This anisotropy is well beyond statistical uncertainties, thereby demonstrating x-ray diffraction signal from the aligned ensemble of isolated DIBN molecules.

Utilizing the iodine-iodine interference of the $I_{\text{YAG}} - I_{\text{NoYAG}}$ pattern, it was investigated whether the iodine-iodine distance could be estimated from the diffraction data. From *ab initio* calculations (GAMESS-US,³³ MP2/6-311G**), a value of 700 pm was predicted for the iodine-iodine distance. Taking into account the wavelength of 620 pm it is clear that the interference features extend to high scattering angles 2Θ , e. g., the first scattering maximum from the iodine-iodine interference appears at $2\Theta = 51^\circ$ which was not covered by the detector; the outer corner of the top pnCCD panel corresponds to $2\Theta = 50^\circ$, i. e., the resolution is low. For this reason, direct methods such as phase-retrieval from the diffraction pattern alone were not applied. Instead, the data was compared to models of different iodine-iodine distances and the best fit of a particular model to the data was estimated as will be explained in the following.

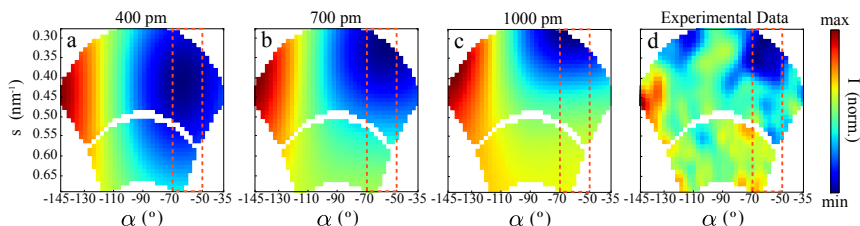


Fig. 6 Diffraction difference $I_{\text{YAG}} - I_{\text{NoYAG}}$ in the (s, α) -representation for simulated and experimental data. The simulated data shows the diffraction-difference $I_{\text{YAG}} - I_{\text{NoYAG}}$ for I–I distances of (a) 400 pm, (b) the theoretically expected I–I distance of 700 pm, and (c) 1000 pm. The experimental data is shown in (d). The dashed red frames mark the azimuthal range $\alpha \in [-70^\circ, -50^\circ]$ along which the $I(s)$ graph is obtained.

Figure 6 shows the diffraction-difference $I_{\text{YAG}} - I_{\text{NoYAG}}$ in a different representation. The (x, y) -coordinates were transformed to (s, α) -coordinates, where $s = \sin \Theta / \lambda$ is the scattering vector and α is the azimuthal angle. Due to the twofold symmetry of the diffraction pattern for rotations about the z -axis, the upper pnCCD was rotated by 180° and “connected” to the bottom edge of the lower pnCCD, thereby extending the range of s -values. Due to the masking of pnCCD regions during the generation of photon hit lists (see Appendix A) the active regions of the two pnCCD panels do not overlap.

Varying the iodine-iodine distance d mainly results in squeezing/stretching of the diffraction minima/maxima in the diffraction pattern. This is most pronounced along the alignment direction $\alpha = -60^\circ$ for the first diffraction minimum in our data. The intensity profile $I(s)$ of the $I_{\text{YAG}} - I_{\text{NoYAG}}$ data along with simulated $I(s)$ profiles for varying iodine-iodine distances is shown as a function

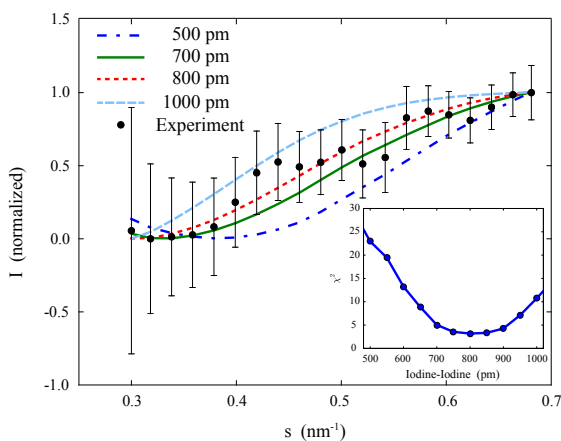


Fig. 7 Comparison of experimentally obtained intensity profiles $I(s)$ along the alignment direction of the diffraction-difference pattern $I_{\text{YAG}} - I_{\text{NoYAG}}$ with simulated profiles. The experimentally obtained $I(s)$ is best fitted (in terms of a χ^2 test) with the model for an iodine-iodine distance of 800 pm. In the inset the test-statistic χ^2 is shown in dependence of the iodine-iodine distance. Figure reproduced from ref. 26.

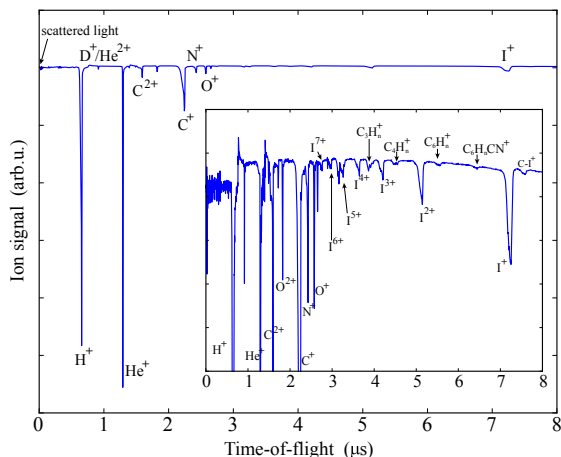


Fig. 8 Time-of-flight spectrum, obtained by probing the molecular beam with the FEL. The inset is a zoom into the vertical axis in order to show the various iodine ions.

of the scattering vector s in Figure 7, averaged over $-70^\circ \leq \alpha \leq -50^\circ$. Each graph is normalized to be independent of the exact molecular beam density M of DIBN molecules, which merely changes the contrast, i. e., the depth of the minimum.

The agreement of the experimental data with a particular model is estimated in terms of a χ^2 -test.⁵² The best fit to the data, corresponding to the minimum χ^2 -value, is obtained for an iodine-iodine distance of 800 pm, see Figure 7. Due to the low resolution at the current experimental parameters, the fitting is not very accurate. Thus, in future experiments the use of shorter wavelengths will be crucial for an accurate determination of structural features with real atomic resolution. At LCLS, the shortest wavelength currently available is $\lambda \approx 130$ pm (photon energy ~ 9.5 keV), while the European XFEL will be able to provide radiation at wavelengths down to $\lambda \approx 50$ pm (photon energy > 24 keV) from its start of operation in the near future.⁵³ In addition, the high repetition rate of 27 000 Hz at European XFEL allows recordance of such diffraction patterns with better statistics in even shorter amounts of time than is currently possible.

Deviations from the equilibrium geometry could be explained by radiation damage effects, i. e., nuclear and/or electronic damage due to the intense XFEL radiation. However, we estimate that radiation damage effects could not be observed in our diffraction data. First, in contrast to previous experiments explicitly investigating the radiation damage induced by strongly focused XFEL beams,^{41,42,54} we deliberately worked out of focus (i. e., at $\omega = 30$ μm), thereby avoiding significant electronic damage effects. Secondly, the wavelength of 620 pm and the range of recorded s -values is insufficient to resolve nuclear motion during the 100 fs x-ray pulses. The reasoning is given in the following.

Figure 8 shows a time-of-flight spectrum, obtained by probing the molecular beam with the FEL. Iodine ions with increasing charge ($I^+ \dots I^{7+}$) appear in the spectrum with decreasing intensity. In particular, singly-charged iodine I^+ is most abundant while fragments with charges higher than I^{7+} are virtually absent

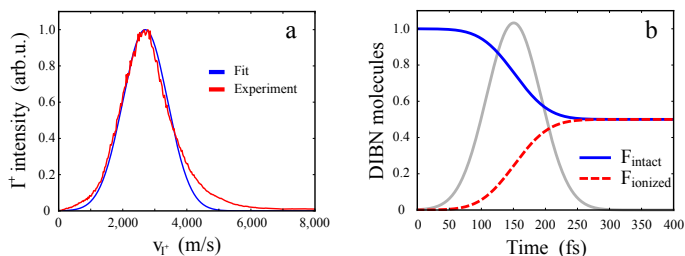


Fig. 9 (a) One-dimensional velocity distribution of I^+ ions, estimated from the momentum distributions as shown in Figure 2. (b) The fractions of intact and ionized DIBN as a function of time for a 100 fs (FWHM) XFEL pulse indicated by the grey line.

in the spectrum. When DIBN is ionized by 2 keV photons, predominantly the M-shell of iodine is accessed and the total photo-ionization cross-section of iodine of $\sigma_{\text{abs}} = 41.92 \text{ pm}^2$ (0.4192 Mbarn) is dominated by the cross-section of the $3p$ and $3d$ subshells. Considering the final charge states reached via Auger decay upon photoabsorption of a 2 keV photon in the $3p$ and $3d$ subshells of iodine, an Auger decay similar to xenon is expected, since the electronic decay processes do not strongly depend on the atomic number. For xenon, multiply charged Xe^{+n} ions are obtained from such a photoionization event,⁵⁵ e. g., an initial $3d$ vacancy in xenon yields Xe^{+4} as the most probable final charge state, while for a $3p$ vacancy, the charge-state distribution is shifted upwards and peaks around Xe^{+7} . The most-probable final charge state has, in both cases, a probability of $\approx 50\%$. Thus, by assuming similar ionization pathways for xenon and iodine, the absorption of a single 2 keV photon by DIBN is likely to result in a charge state distribution of DIBN peaking at DIBN^{+4} or higher charges. Hence, iodine charge states of I^{+1} to I^{+7} could be entirely due to absorption of only a single photon. We conclude that typically one photon is absorbed per molecule. In the following, absorption of two or more photons is neglected.

For the moderate fluence conditions in our experiment, the probability p_{abs} for single-photon absorption of DIBN can be calculated based on the photoabsorption cross section of atomic iodine $\sigma_{\text{abs}} = 41.92 \text{ pm}^2$ (0.4192 Mbarn).⁵⁶ Taking into account the number of photons $N_{\text{photons}} = 4.375 \cdot 10^{12}$ and the interaction area $A_0 = 7.068 \cdot 10^{-10} \text{ m}^2$ ($706.8 \mu\text{m}^2$), the probability for photoabsorption of a 2 keV photon by a single iodine atom is $p_{\text{abs}} = 0.25$, hence the probability for a DIBN molecule (i. e., two iodine atoms) is 0.5, i. e., half of the DIBN molecules absorb an x-ray photon, and, eventually, become multiply ionized by Auger relaxation and fragment due to Coulomb explosion.

We estimate the influence of scattering from fragmenting DIBN on the diffraction pattern in terms of a simple mechanical model concerning only nuclear damage, i. e., motion of ionic fragments happening during the 100 fs (FWHM) x-ray pulse due to Coulomb explosion. The effective spatial distribution of the two main scattering centers, i. e., the two iodine atoms, seen by the entire FEL during a single shot is estimated, taking into account the gradual ionization during the course of the FEL pulse, the total amount of ionization, and the velocity distribution obtained from the measured momentum distributions of I^+ ions.

A one-dimensional cut along the x -axis through the momentum distribution in Figure 2 is shown in Figure 9. It represents the measured I^+ -velocity distribution v_{I^+} in the laboratory frame. The data can be approximated by a Gaussian distribution with mean $\mu = 2700$ m/s and width $\sigma = 700$ m/s. Considering momentum conservation, the distribution of the relative velocities v_{I-I} of the two iodine atoms is then given by a Gaussian distribution with $\mu_v = 4200$ m/s and $\sigma_v = 1090$ m/s. Since a complete velocity distribution of all ions has not been determined experimentally, this model assumes fragmentation into I^+ and $[C_7H_3IN]^{+n}$.[†] The resulting velocity distribution of I^+ fragments from ionized molecules is

$$v_{I-I} = C \cdot \exp\left(-\frac{(v - \mu_v)^2}{2\sigma_v^2}\right) \quad (6)$$

with the normalization constant C (such that $\int v_{I-I} dv = 1$). This translates into a spatial distribution of I–I distances $s(\Delta t, d)$ by the substitution $d = v \Delta t$, with the period $\Delta t = t - t_i$ between ionization time t_i and observation time t .

At each time t the probability for photoabsorption and ionization of molecules is $f_{\text{ionized}}(t) = I_{\text{FEL}}(t) \cdot \sigma_{\text{abs}} \cdot N/A_0$ with the FEL intensity $I_{\text{FEL}}(t)$, the photoabsorption cross section σ_{abs} , the number of molecules N , and the interaction area A_0 . N/A_0 can be substituted by $M \cdot l$ with the molecular beam density M and the length of the interaction volume in z -direction l (see section 3), hence $f_{\text{ionized}}(t) = I_{\text{FEL}}(t) \cdot \sigma_{\text{abs}} \cdot M \cdot l$. For each time t , the distribution of I–I distances is given as the sum of intact-molecules with distances d_0 and the distributions of all previously ionized molecules

$$s(t, d) = F_{\text{intact}}(t) \cdot N \cdot s(0, d_0) + \sum_{t_i=0}^t s(t - t_i, d) \cdot f_{\text{ionized}}(t_i) \quad (7)$$

with the fraction $F_{\text{intact}}(t)$ of intact molecules at time t and the fraction $f_{\text{ionized}}(t_i)$ of molecules ionized at a certain particular time t_i with the property that $\sum_{t_i=0}^t f_{\text{ionized}}(t_i) = F_{\text{ionized}}(t)$, see Figure 9 b.

The spatial distribution of I–I distances as seen by the FEL pulse is the sum over $s(t, d)$ for all times, weighted by the instantaneous normalized FEL intensity $I_{\text{FEL}}^{\text{norm}}(t) = I_{\text{FEL}}(t) / \sum I_{\text{FEL}}(t)$:

$$S(d) = \sum_t s(t, d) \cdot I_{\text{FEL}}^{\text{norm}}(t) \quad (8)$$

This distribution is shown in Figure 10 a. The corresponding cumulative distribution of I–I distances is illustrated by the solid blue line in Figure 10 b. The latter gives the amount of molecules with I–I distances equal to or less than the given distance summed over the entire FEL pulse, e. g., 75 % of the elastically scattered photons originate from scattering at intact molecules (i. e., I–I-distance at equilibrium distance of 700 pm) and another 15 % (20 %) of the diffraction signal

[†] We note that this model contains two simplifications: First, the time for acceleration of the fragments as well as the time for ionization, i. e., the finite delay for Auger decay and subsequent charge rearrangement after photoabsorption was not taken into account (i. e., set to zero). Therefore, our model overestimates the atomic displacements. However, this is partly counteracted by the fact that higher charged I^{+n} fragments recoil faster than I^+ and hence lead to larger atomic displacements, which is not considered, because these momentum distributions of higher charged I^{+n} fragments were not measured.

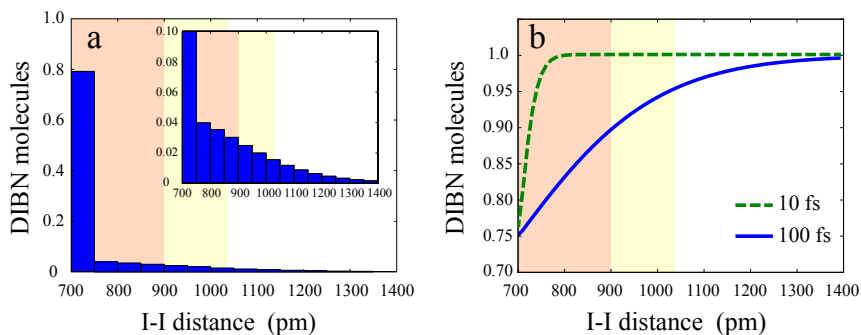


Fig. 10 (a) Histogram of $S(d)$, visualizing the fraction of molecules in different distance intervals, as seen by the 100 fs (FWHM) FEL pulse (blue). (b) The cumulative distribution of $S(d)$ (for smaller stepsize in I–I-distance). I–I distances that are less than 200 pm (330 pm) longer than the 700 pm equilibrium distance are marked by the red (yellow) shaded regions. The dashed green graph in (b) is for a theoretical case of a 10 fs pulse.

originates from scattering of molecules corresponding to I–I distances that are less than 200 pm (330 pm) longer than the 700 pm equilibrium distance. These distances correspond to the red (yellow) shaded regions in Figure 10. These damaged molecules might contribute to the experimentally determined elongated I–I distance of 800 pm in the minimum of the χ^2 -fit. However, since the range of s -values (scattering vectors) covered is too small, these effects cannot be fully resolved in the current experiment with 620 pm wavelength radiation. Further suppressing such effects on the diffraction pattern could, for instance, be accomplished by using shorter pulses. For 10 fs practically no damage would be observed and even for the same pulse energy 95 % of the molecules would be at equilibrium distance to within 40 pm.

5 Conclusion and Outlook

We experimentally demonstrated coherent x-ray diffractive imaging of laser-aligned gas-phase samples of the prototypical complex molecule 2,5-diiodobenzonitrile at the LCLS XFEL. This x-ray diffraction experiment resembles Young's double slit experiment on the atomic level due to the two-center interference of the two heavy iodine atoms. We implemented a state-of-the-art molecular beam setup in the CAMP experimental chamber at the AMO beamline of LCLS, utilized quantum-state selection of a cold molecular beam, and demonstrated the preparation of a strongly aligned ensemble of isolated gas-phase molecules. The controlled samples of DIBN were probed by the x-ray pulses in order to measure x-ray diffraction from these ensembles of aligned DIBN. Exploiting the high spectral resolution of the pnCCD detectors, we could successfully retrieve single scattered photons above noise and derive the molecular diffraction patterns from the weak and noisy signals. On average, 0.2 photons/shot were recorded on the camera. However, the angular structures contained in the diffraction patterns are well beyond experimental noise, i. e., we

succeeded to observe the two-center interference of the two heavy iodine atoms in the diffraction pattern which confirms the observation of a successful diffraction measurement from aligned DIBN. Even despite the limited resolution, i. e., the long wavelength and the correspondingly limited range of scattering vectors s recorded, the heavy-atom distance was experimentally obtained and it is consistent with the computed molecular structure. Future experiments toward atomic resolution imaging will have to use shorter wavelength and collect diffraction data at higher resolution.

Our experiment confirms the feasibility of coherent x-ray diffractive imaging of small isolated gas-phase molecules and hence provides a first step towards single-molecule imaging at atomic resolution. Our controlled delivery approach is capable to provide three-dimensional alignment and orientation,^{11,14,57} which would allow the determination of the 3D molecular structure using a tomographic approach similar to electron diffraction¹⁵ or photoelectron tomography.⁵⁸

Envisioned future experiments plan to make use of the unique short pulses of the XFELs in order to conduct fs pump-probe experiments in order to investigate ultrafast structural dynamics during, e. g., chemical reactions and open up a new field for experiments in femtochemistry and molecular dynamics. For the recording of molecular movies of ultrafast dynamics, x rays offer several advantages over electrons: x-ray pulses do not suffer from space-charge broadening of pulses nor from pump-probe velocity mismatch.^{59,60} Hence, x-ray pulses from XFELs will permit better temporal resolution. Pulses as short as a 2–5 fs are already routinely created at XFELs,^{61,62} and attosecond x-ray pulses are discussed.⁶³ These short pulses will allow the observation of the fastest nuclear motion and, moreover, the investigation of ultrafast electron dynamics, such as charge migration and charge transfer processes in molecular and chemical processes.^{64,65}

We analyzed how damage effects can be avoided by using short pulses of low fluence at high repetition rates, which will be available at future XFELs, such as the upcoming European XFEL that will operate at 27 000 x-ray pulses/second. Our approach is suitable to study larger molecules provided moderately dense molecular beams of these samples can be generated. Hence, it should be applicable for coherent diffractive imaging of isolated biomolecules, as envisioned for a long time.^{5,6,66,67}

Acknowledgements

We thank Marcus Adolph, Andrew Aquila, Saša Bajt, Carl Caleman, Nicola Copola, Tjark Delmas, Holger Fleckenstein, Tais Gorkhover, Lars Gumprecht, Andreas Hartmann, Günter Hauser, Peter Holl, Andre Hömke, Faton Krasniqi, Gerard Meijer, Robert Moshhammer, Christian Reich, Robin Santra, Ilme Schlichting, Carlo Schmidt, Sebastian Schorb, Joachim Schulz, Heike Soltau, John C. H. Spence, Lothar Strüder, Joachim Ullrich, Marc J. J. Vrakking, and Cornelia Wunderer for help in preparing or performing the measurements.

Parts of this research were carried out at the Linac Coherent Light Source (LCLS) at the SLAC National Accelerator Laboratory. LCLS is an Office of Science User Facility operated for the U. S. Department of Energy Office of Science by Stanford University. We acknowledge the Max Planck Society for funding the development and operation of the CAMP instrument within the ASG at CFEL.

A.Ro. acknowledges the research program of the "Stichting voor Fundamenteel Onderzoek der Materie", which is financially supported by the "Nederlandse organisatie voor Wetenschappelijk Onderzoek". H. S. acknowledges support from the Carlsberg Foundation. P. J. acknowledges support from the Swedish Research Council and the Swedish Foundation for Strategic Research. H.N.C. acknowledges NSF STC award 1231306. A.Ru. acknowledges support from the Chemical Sciences, Geosciences, and Biosciences Division, Office of Basic Energy Sciences, Office of Science, US Department of Energy. D. R. acknowledges support from the Helmholtz Gemeinschaft through the Young Investigator Program. This work has been supported by the excellence cluster "The Hamburg Center for Ultrafast Imaging – Structure, Dynamics and Control of Matter at the Atomic Scale" of the Deutsche Forschungsgemeinschaft.

Notes

¹Present address: Bruker AXS GmbH, Karlsruhe, Germany

²Present address: ARC Centre of Excellence for Coherent X-ray Science, School of Physics, The University of Melbourne, Australia

³Present address: Physikalisch-Technische Bundesanstalt, Bundesallee 100, 38116 Braunschweig, Germany

⁴Present address: Stanford PULSE Institute, SLAC National Accelerator Laboratory, 2575 Sand Hill Road, Menlo Park, California 94025, USA

⁵Present address: European X-ray Free Electron Laser (XFEL) GmbH, 22761 Hamburg, Germany

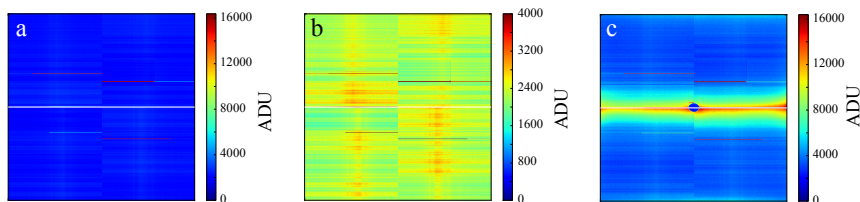


Fig. 11 Single shot raw data frames of an example dataset for the NoYAG case (a,b) and the YAG case (c).

Appendix A Data acquisition and conditioning of x-ray diffraction data

X-ray diffraction data was recorded by the pnCCD photon detectors with the LCLS operating at 60 Hz. The YAG was operating at 30 Hz, hence single-shot YAG and NoYAG data was recorded in an alternating manner. The YAG and LCLS laser were propagating collinearly (see Figure 1) which resulted in severe background levels from the YAG on the pnCCD despite the filters. This background as well as camera artifacts, known from dark frame measurements, were subtracted from the single shot data. The necessary single-photon counting required operation of the pnCCD cameras at the highest possible gain in order to give a good separation of 2 keV and optical and NIR photons (the latter from the YAG). Spectroscopic discrimination of rare events, i. e., single 2 keV x-ray photons, could be performed due to the high energy resolution of the pnCCD camera.²⁷ In this chapter we describe the steps necessary to correct the single-shot diffraction data for all artifacts and backgrounds. All processing of the data was performed using the CFEL-ASG Software Suite (CASS).³²

Figure 11 shows typical examples of single shot raw data frames for both panels of the pnCCD camera for (a, b) NoYAG and (c) YAG, which contain many artifacts. The measured pnCCD signals are given in ADU (analog-to-digital unit). The most significant difference between NoYAG and YAG data is the region of partly saturated signal at the inner edges of the two pnCCD panels in the YAG case. These signals are based on imperfect shielding of both pnCCD panels from near-infrared (NIR) photons especially at their respective edges.[‡] This contribution to the experimental background is referred to as “YAG background”. Furthermore, the single shot data contains pnCCD based artifacts such as offset- and gain variations, “hot pixels” or even “hot rows/channels”, and time-dependent readout fluctuations called “common mode” (during read out of the pnCCDs, charges are shifted towards the ASIC along the horizontal direction). The pnCCD consist of 16 CAMEX modules.[§] The pnCCD-based artifacts and distinct offset within the 16 CAMEX modules become more obvious when zooming into the colorscale, see Figure 11 (b).[¶]

[‡] The charge created by a single YAG photon is less than a 1/500th of the charge created by a single 2 keV x-ray photon. However, due to the high YAG intensity, many YAG photons pile up in a single pixel, especially in the regions not shielded thoroughly by the filters.

[§] For a description of the CAMEX modules, see references 27, 28.

[¶] Although there is a channel-specific offset and gain variation, all channels within the same CAMEX have similar gain and the difference of the channel-specific gain between distinct CAMEX is more

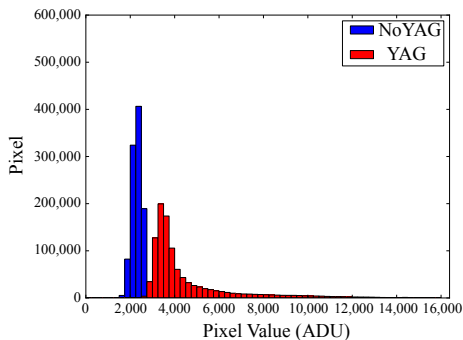


Fig. 12 Spectra for the single shot data frames given in Figure 11 a, c; see text for details.

In our experiment, scattering from ensembles of isolated molecules is very weak; in particular the probability for two or more x-ray photons scattered to the same pixel on the detector within the same single shot is negligible small. Therefore, single x-ray photon hits could be found by spectroscopic, i. e., energy-dependent discrimination of single-shot data which was corrected for all pnCCD artifacts and the YAG background. The measured ADU value is proportional to the energy and a single 2 keV x-ray photon corresponds to a value of ≈ 2600 ADU.

Figure 12 shows histograms for the 1024×1024 pnCCD values of the single shot data frames given in Figure 11 (a–c). There is a constant offset of ≈ 2400 ADU in most pixels and in both cases (YAG and NoYAG). In the YAG case, in addition to the pnCCD-based offset, there is the huge background at the inner (and outer edges) of the two pnCCD panels, resulting in a shift of the spectrum towards higher values.

The YAG background was utilized to reliably distinguish single-shot YAG from single-shot NoYAG data. Figure 13 shows a histogram of the integrated pnCCD signals for single YAG/NoYAG shots for an example dataset, illustrating the clear separation of YAG and NoYAG shots. The variation in the YAG case is

pronounced than the gain variation within one CAMEX.

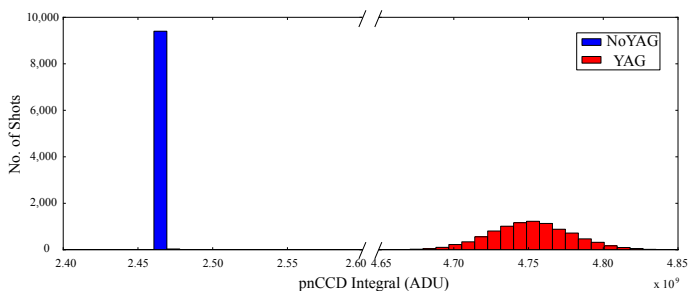


Fig. 13 Histogram of the total integrated value of individual YAG/NoYAG data for an example dataset containing 9451 shots with YAG off (NoYAG) and 9449 shots with YAG on (YAG).

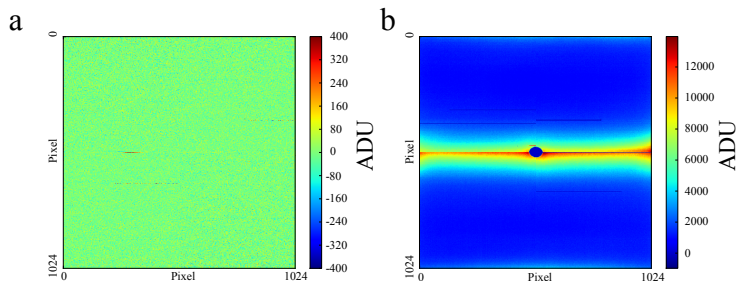


Fig. 14 Single shot pnCCD data frames, corrected for channel-dependent offset and common mode.

due to the YAG intensity, varying on a shot-to-shot level.

First during the data conditioning process, single-shot YAG and NoYAG data was separated based on the integrated pnCCD signals. Then, the data was corrected for offset by subtracting an offset map, the latter obtained from averaging single shot pnCCD data under “dark” conditions. The common mode was corrected for by subtracting the median value along each vertical row from this row, separately for the upper and lower pnCCD panel. Figure 14 shows the resulting frames for the YAG and NoYAG case. The channel-specific offset variation was successfully corrected for. The NoYAG data is close to 0 value for almost every pixel while the YAG data still contains the severe background from the YAG.

The YAG background scattering was corrected for by subtracting a averaged YAG data frame, scaled to match the total intensity of the particular individual single-shot data frame, from the individual single-shot YAG frame. This method works reliable since the total YAG intensity is varying on a shot-to-shot level but the spatial distribution of the YAG on the pnCCD is independent of a certain shot (i. e., it can be scaled by a single number).

As a result from the steps mentioned above, the single-shot data frames were corrected for all backgrounds and artifacts except rare events such as single 2 keV x-ray photons scattered from the molecular sample. These photons, at ≈ 2600 ADU, were found by thresholding the background-corrected data frames and considering the charge spread of the x-ray photons: a 2 keV photon absorbed in the pnCCD creates a charge cloud which can cross the barrier of a single pixel and hence can give signals in two (or more) adjacent pixels. At 2 keV, almost all photon hits are single- or double-pixel hits (the latter is the case in which the charge cloud diffuses into a single neighboring pixel adjacent to the pixel where the photon is initially absorbed). This is justified by the experimental results, where 64 % of all x-ray attributed hits are single-pixel hits, 35 % are double-pixel hits while < 1 % make up for the rest. These photon hits were found by thresholding the background-corrected single-shot YAG and NoYAG data frames and combining adjacent pixels exceeding the threshold of 500 ADU. The x-ray hits found by this procedure were written to a list containing the coordinates, ADU value, and number of pixels the hit was combined from. By limiting the number of pixels a hit can be made of to six, rare events such as high energy particles impinging on the detector were neglected. Then, corrections for channel-dependent gain and charge-transfer-efficiency were applied to the energy values of the pho-

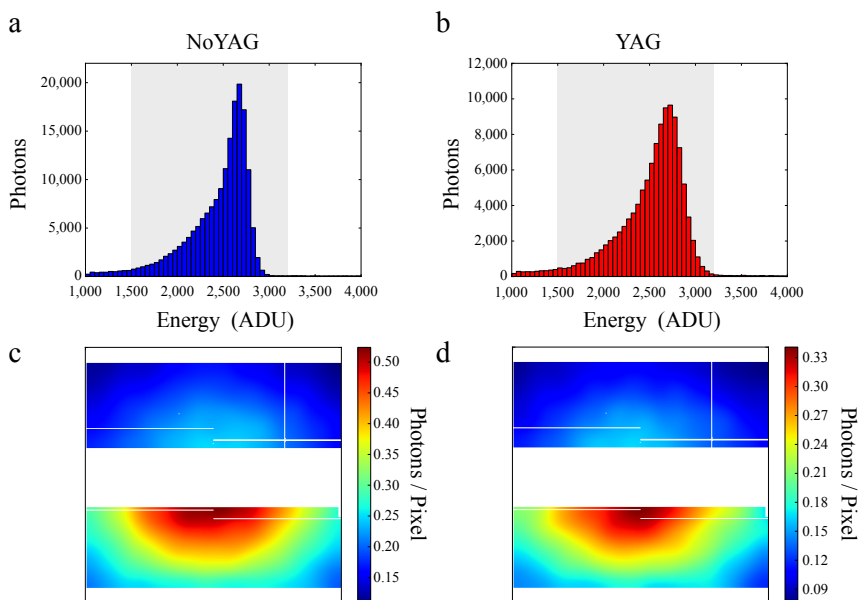


Fig. 15 Spectra of the hits for NoYAG (a) and YAG (b) for hits made up out of 1–2 pixels; spatial intensity distributions I_{YAG} , I_{NoYAG} of these hits in the energy interval 1500–3200 ADU (c, d), i. e., the “diffraction patterns”. The raw data was convolved with a gaussian kernel.

ton hits (although these corrections didn’t affect the spatial distribution and also have almost no effect on the spectral distribution of the hits as well). Photon hits for certain regions of pixels were always neglected. This included “hot pixel” regions as well as the parts of the pnCCD that were (completely or nearly) saturated by YAG photons. The latter regions showed a high fluctuation of signal and, therefore, could not be thresholded successfully.

Figure 15 a, b show spectra of all photon hits from the NoYAG (a) and YAG (b) data. The spectrum is peaked at 2600 ADU, thereby matching expectations. The width of the peak can be attributed the energy resolution of the pnCCDs, the photon energy jitter of LCLS, and to the event recombination of double pixel hits (the latter being the major contribution to the broadening of the spectrum).

In the energy interval 1500–3200 ADU there are 172 499 photons for the NoYAG and 111 560 photons for the YAG data which are used for data analysis. The data was obtained from 842 722 shots (NoYAG) and 563 453 shots (YAG) respectively, hence the average hit rate on the whole pnCCD detector was 0.204 (0.197) photons/shot for the NoYAG (YAG) data. The spatial distribution of these photon hits, i. e., the diffraction patterns I_{NoYAG} and I_{YAG} , are shown in Figure 15 c, d and are analyzed as described in section 4.

References

- 1 R. Neutze, R. Wouts, D. van der Spoel, E. Weckert and J. Hajdu, *Nature*, 2000, **406**, 752–757.

-
- 2 M. M. Seibert, T. Ekeberg, F. R. N. C. Maia, M. Svenda, J. Andreasson, O. Jönsson, D. Odić, B. Iwan, A. Rocker, D. Westphal, M. Hantke, D. P. Deponte, A. Barty, J. Schulz, L. Gumprecht, N. Coppola, A. Aquila, M. Liang, T. A. White, A. Martin, C. Caleman, S. Stern, C. Abergel, V. Seltzer, J.-M. Claverie, C. Bostedt, J. D. Bozek, S. Boutet, A. A. Miahnahri, M. Messerschmidt, J. Krzywinski, G. Williams, K. O. Hodgson, M. J. Bogan, C. Y. Hampton, R. G. Sierra, D. Starodub, I. Andersson, S. Bajt, M. Barthelmess, J. C. H. Spence, P. Fromme, U. Weierstall, R. Kirian, M. Hunter, R. B. Doak, S. Marchesini, S. P. Hau-Riege, M. Frank, R. L. Shoeman, L. Lomb, S. W. Epp, R. Hartmann, D. Rolles, A. Rudenko, C. Schmidt, L. Foucar, N. Kimmel, P. Holl, B. Rudek, B. Erk, A. Hömke, C. Reich, D. Pietschner, G. Weidenspointner, L. Strüder, G. Hauser, H. Gorke, J. Ullrich, I. Schlichting, S. Herrmann, G. Schaller, F. Schopper, H. Soltau, K.-U. Kühnel, R. Andritschke, C.-D. Schröter, F. Krasniqi, M. Bott, S. Schorb, D. Rupp, M. Adolph, T. Gorkhover, H. Hirsemann, G. Potdevin, H. Graafsma, B. Nilsson, H. N. Chapman and J. Hajdu, *Nature*, 2011, **470**, 78.
 - 3 H. N. Chapman, P. Fromme, A. Barty, T. A. White, R. A. Kirian, A. Aquila, M. S. Hunter, J. Schulz, D. P. Deponte, U. Weierstall, R. B. Doak, F. R. N. C. Maia, A. V. Martin, I. Schlichting, L. Lomb, N. Coppola, R. L. Shoeman, S. W. Epp, R. Hartmann, D. Rolles, A. Rudenko, L. Foucar, N. Kimmel, G. Weidenspointner, P. Holl, M. Liang, M. Barthelmess, C. Caleman, S. Boutet, M. J. Bogan, J. Krzywinski, C. Bostedt, S. Bajt, L. Gumprecht, B. Rudek, B. Erk, C. Schmidt, A. Hömke, C. Reich, D. Pietschner, L. Strüder, G. Hauser, H. Gorke, J. Ullrich, S. Herrmann, G. Schaller, F. Schopper, H. Soltau, K.-U. Kühnel, M. Messerschmidt, J. D. Bozek, S. P. Hau-Riege, M. Frank, C. Y. Hampton, R. G. Sierra, D. Starodub, G. J. Williams, J. Hajdu, N. Timneanu, M. M. Seibert, J. Andreasson, A. Rocker, O. Jönsson, M. Svenda, S. Stern, K. Nass, R. Andritschke, C.-D. Schröter, F. Krasniqi, M. Bott, K. E. Schmidt, X. Wang, I. Grotjohann, J. M. Holton, T. R. M. Barends, R. Neutze, S. Marchesini, R. Fromme, S. Schorb, D. Rupp, M. Adolph, T. Gorkhover, I. Andersson, H. Hirsemann, G. Potdevin, H. Graafsma, B. Nilsson and J. C. H. Spence, *Nature*, 2011, **470**, 73.
 - 4 M. Chergui and A. H. Zewail, *Chemphyschem*, 2009, **10**, 28–43.
 - 5 A. Barty, J. Küpper and H. N. Chapman, *Annu. Rev. Phys. Chem.*, 2013, **64**, 415–435.
 - 6 J. C. H. Spence and R. B. Doak, *Phys. Rev. Lett.*, 2004, **92**, 198102.
 - 7 F. Filsinger, G. Meijer, H. Stapelfeldt, H. Chapman and J. Küpper, *Phys. Chem. Chem. Phys.*, 2011, **13**, 2076–2087.
 - 8 N.-T. D. Loh and V. Elser, *Phys. Rev. E*, 2009, **80**, 026705.
 - 9 R. Fung, V. Shneerson, D. Saldin and A. Ourmazd, *Nat. Phys.*, 2009, **5**, 64–67.
 - 10 O. M. Yefanov and I. A. Vartanyants, *J. Phys. B*, 2013, **46**, 164013.
 - 11 J. J. Larsen, K. Hald, N. Bjerre, H. Stapelfeldt and T. Seideman, *Phys. Rev. Lett.*, 2000, **85**, 2470–2473.
 - 12 H. Stapelfeldt and T. Seideman, *Rev. Mod. Phys.*, 2003, **75**, 543–557.
 - 13 L. Holmegaard, J. H. Nielsen, I. Nevo, H. Stapelfeldt, F. Filsinger, J. Küpper and G. Meijer, *Phys. Rev. Lett.*, 2009, **102**, 023001.

- 14 I. Nevo, L. Holmegaard, J. H. Nielsen, J. L. Hansen, H. Stapelfeldt, F. Filsinger, G. Meijer and J. Küpper, *Phys. Chem. Chem. Phys.*, 2009, **11**, 9912–9918.
- 15 C. J. Hensley, J. Yang and M. Centurion, *Phys. Rev. Lett.*, 2012, **109**, 133202.
- 16 R. Boll, D. Anielski, C. Bostedt, J. D. Bozek, L. Christensen, R. Coffee, S. De, P. Declava, S. W. Epp, B. Erk, L. Foucar, F. Krasniqi, J. Küpper, A. Rouzée, B. Rudek, A. Rudenko, S. Schorb, H. Stapelfeldt, M. Stener, S. Stern, S. Techert, S. Trippel, M. J. J. Vrakking, J. Ullrich and D. Rolles, *Phys. Rev. A*, 2013, **88**, 061402.
- 17 R. Boll, D. Anielski, C. Bostedt, J. D. Bozek, L. Christensen, R. Coffee, S. De, P. Declava, S. W. Epp, B. Erk, L. Foucar, F. Krasniqi, J. Küpper, A. Rouzée, B. Rudek, A. Rudenko, S. Schorb, H. Stapelfeldt, M. Stener, S. Stern, S. Techert, S. Trippel, M. Vrakking, J. Ullrich and D. Rolles, *Faraday Disc.*, 2014, **171**, year.
- 18 D. Rolles, R. Boll, M. Adolph, A. Aquila, C. Bostedt, J. Bozek, H. Chapman, R. Coffee, N. Coppola, P. Declava, T. Delmas, S. Epp, B. Erk, F. Filsinger, L. Foucar, L. Gumprecht, A. Hömke, T. Gorkhover, L. Holmegaard, P. Johnsson, C. Kaiser, F. Krasniqi, K.-U. Kühnel, J. Maurer, M. Messerschmidt, R. Moshhammer, W. Quevedo, I. Rajkovic, A. Rouzée, B. Rudek, I. Schlichting, C. Schmidt, S. Schorb, C. D. Schröter, J. Schulz, H. Stapelfeldt, M. Stener, S. Stern, S. Techert, J. Thøgersen, M. J. J. Vrakking, A. Rudenko, J. Küpper and J. Ullrich, *J. Phys. B*, 2014.
- 19 G. von Helden, T. Wyttenbach and M. T. Bowers, *Science*, 1995, **267**, 1483–1485.
- 20 S. Trippel, Y.-P. Chang, S. Stern, T. Mullins, L. Holmegaard and J. Küpper, *Phys. Rev. A*, 2012, **86**, 033202.
- 21 F. Filsinger, U. Erlekm, G. von Helden, J. Küpper and G. Meijer, *Phys. Rev. Lett.*, 2008, **100**, 133003.
- 22 F. Filsinger, J. Küpper, G. Meijer, J. L. Hansen, J. Maurer, J. H. Nielsen, L. Holmegaard and H. Stapelfeldt, *Angew. Chem. Int. Ed.*, 2009, **48**, 6900–6902.
- 23 T. Kierspel, D. A. Horke, Y.-P. Chang and J. Küpper, *Chem. Phys. Lett.*, 2014, **591**, 130–132.
- 24 F. Filsinger, J. Küpper, G. Meijer, L. Holmegaard, J. H. Nielsen, I. Nevo, J. L. Hansen and H. Stapelfeldt, *J. Chem. Phys.*, 2009, **131**, 064309.
- 25 S. Trippel, T. Mullins, N. L. M. Müller, J. S. Kienitz, K. Długolecki and J. Küpper, *Mol. Phys.*, 2013, **111**, 1738.
- 26 J. Küpper, S. Stern, L. Holmegaard, F. Filsinger, A. Rouzée, A. Rudenko, P. Johnsson, A. V. Martin, M. Adolph, A. Aquila, S. Bajt, A. Barty, C. Bostedt, J. Bozek, C. Caleman, R. Coffee, N. Coppola, T. Delmas, S. Epp, B. Erk, L. Foucar, T. Gorkhover, L. Gumprecht, A. Hartmann, R. Hartmann, G. Hauser, P. Holl, A. Hömke, N. Kimmel, F. Krasniqi, K.-U. Kühnel, J. Maurer, M. Messerschmidt, R. Moshhammer, C. Reich, B. Rudek, R. Santra, I. Schlichting, C. Schmidt, S. Schorb, J. Schulz, H. Soltau, J. C. H. Spence, D. Starodub, L. Strüder, J. Thøgersen, M. J. J. Vrakking, G. Weidenspointner, T. A. White, C. Wunderer, G. Meijer, J. Ullrich, H. Stapelfeldt, D. Rolles and H. N. Chapman, *Phys. Rev. Lett.*, 2014, **112**, 083002.

-
- 27 L. Strüder, S. Epp, D. Rolles, R. Hartmann, P. Holl, G. Lutz, H. Soltau, R. Eckart, C. Reich, K. Heinzinger, C. Thamm, A. Rudenko, F. Krasniqi, K. Kühnel, C. Bauer, C.-D. Schroeter, R. Moshhammer, S. Techert, D. Miessner, M. Porro, O. Haelker, N. Meidinger, N. Kimmel, R. Andritschke, F. Schopper, G. Weidenspointner, A. Ziegler, D. Pietschner, S. Herrmann, U. Pietsch, A. Walenta, W. Leitenberger, C. Bostedt, T. Moeller, D. Rupp, M. Adolph, H. Graafsma, H. Hirsemann, K. Gaertner, R. Richter, L. Foucar, R. L. Shoeman, I. Schlichting and J. Ullrich, *Nucl. Instrum. Meth. A*, 2010, **614**, 483–496.
- 28 R. Hartmann, S. Epp, S. Herrmann, P. Holl, N. Meidinger, C. Reich, D. Rolles, H. Soltau, L. Strüder, J. Ullrich and G. Weidenspointner, Nuclear Science Symposium Conference Record, 2008. NSS '08. IEEE, 2008, pp. 2590–2595.
- 29 J. D. Bozek, *Eur. Phys. J. Special Topics*, 2009, **169**, 129–132.
- 30 C. Bostedt, J. D. Bozek, P. H. Bucksbaum, R. N. Coffee, J. B. Hastings, Z. Huang, R. W. Lee, S. Schorb, J. N. Corlett, P. Denes, P. Emma, R. W. Falcone, R. W. Schoenlein, G. Doumy, E. P. Kanter, B. Kraessig, S. Southworth, L. Young, L. Fang, M. Hoener, N. Berrah, C. Roedig and L. F. DiMauro, *J. Phys. B*, 2013, **46**, 164003.
- 31 P. Emma, R. Akre, J. Arthur, R. Bionta, C. Bostedt, J. Bozek, A. Brachmann, P. Bucksbaum, R. Coffee, F. J. Decker, Y. Ding, D. Dowell, S. Edstrom, A. Fisher, J. Frisch, S. Gilevich, J. Hastings, G. Hays, P. Hering, Z. Huang, R. Iverson, H. Loos, M. Messerschmidt, A. Miahnahri, S. Moeller, H. D. Nuhn, G. Pile, D. Ratner, J. Rzepiela, D. Schultz, T. Smith, P. Stefan, H. Tompkins, J. Turner, J. Welch, W. White, J. Wu, G. Yocky and J. Galayda, *Nat. Photon.*, 2010, **4**, 641–647.
- 32 L. Foucar, A. Barty, N. Coppola, R. Hartmann, P. Holl, U. Hoppe, S. Kassemeyer, N. Kimmel, J. Küpper, M. Scholz, S. Techert, T. A. White, L. Strüder and J. Ullrich, *Comp. Phys. Comm.*, 2012, **183**, 2207–2213.
- 33 M. W. Schmidt, K. K. Baldridge, J. A. Boatz, S. T. Elbert, M. S. Gordon, J. H. Jensen, S. Koseki, N. Matsunaga, K. A. Nguyen, S. Su, T. L. Windus, M. Dupuis and J. A. Montgomery, *J. Comput. Chem.*, 1993, **14**, 1347–1363.
- 34 U. Even, J. Jortner, D. Noy, N. Lavie and N. Cossart-Magos, *J. Chem. Phys.*, 2000, **112**, 8068–8071.
- 35 *Atomic and Molecular Beam Methods*, ed. G. Scoles, Oxford University Press, New York, 1988.
- 36 K. Luria, W. Christen and U. Even, *J. Phys. Chem. A*, 2011, **115**, 7362–7367.
- 37 S. Düsterer, P. Radcliffe, C. Bostedt, J. Bozek, A. L. Cavalieri, R. Coffee, J. T. Costello, D. Cubaynes, L. F. DiMauro, Y. Ding, G. Doumy, F. Grüner, W. Helml, W. Schweinberger, R. Kienberger, A. R. Maier, M. Messerschmidt, V. Richardson, C. Roedig, T. Tschentscher and M. Meyer, *New J. Phys.*, 2011, **13**, 093024.
- 38 U. Lorenz, N. M. Kabachnik, E. Weckert and I. A. Vartanyants, *Phys. Rev. E*, 2012, **86**, 051911.
- 39 B. Ziaja, H. N. Chapman, R. Fäustlin, S. Hau-Riege, Z. Jurek, A. V. Martin, S. Toleikis, F. Wang, E. Weckert and R. Santra, *New J. Phys.*, 2012, **14**, 115015.

-
- 40 A. Fratolocci and G. Ruocco, *Phys. Rev. Lett.*, 2011, **106**, 105504.
- 41 B. Erk, D. Rolles, L. Foucar, B. Rudek, S. W. Epp, M. Cryle, C. Bostedt, S. Schorb, J. Bozek, A. Rouzee, A. Hundertmark, T. Marchenko, M. Simon, F. Filsinger, L. Christensen, S. De, S. Trippel, J. Küpper, H. Stapelfeldt, S. Wada, K. Ueda, M. Swiggers, M. Messerschmidt, C. D. Schroter, R. Moshhammer, I. Schlichting, J. Ullrich and A. Rudenko, *Phys. Rev. Lett.*, 2013, **110**, 053003.
- 42 B. Rudek, S.-K. Son, L. Foucar, S.-W. Epp, B. Erk, R. Hartmann, M. Adolph, R. Andritschke, A. Aquila, N. Berrah, C. Bostedt, N. Bozek, Johnand Coppola, F. Filsinger, H. Gorke, T. Gorkhover, H. Graafsma, L. Gumprecht, A. Hartmann, G. Hauser, S. Herrmann, H. Hirsemann, P. Holl, A. Hömke, L. Journal, C. Kaiser, N. Kimmel, F. Krasniqi, K.-U. Kühnel, M. Matyssek, M. Messerschmidt, D. Miesner, T. Möller, R. Moshhammer, K. Nagaya, B. Nilsson, G. Potdevin, D. Pietschner, C. Reich, D. Rupp, G. Schaller, I. Schlichting, C. Schmidt, F. Schopper, S. Schorb, C.-D. Schröter, J. Schulz, M. Simon, H. Soltau, L. Strüder, K. Ueda, G. Weidenspointner, R. Santra, J. Ullrich, A. Rudenko and D. Rolles, *Nat. Photon.*, 2012, **6**, 858–865.
- 43 W. Wiley and I. McLaren, *Rev. Sci. Instrum.*, 1955, **26**, 1150–1157.
- 44 Y.-P. Chang, F. Filsinger, B. Sartakov and J. Küpper, *Comp. Phys. Comm.*, 2014, **185**, 339–49.
- 45 J. J. Larsen, H. Sakai, C. P. Safvan, I. Wendt-Larsen and H. Stapelfeldt, *J. Chem. Phys.*, 1999, **111**, 7774.
- 46 J. Als-Nielsen and D. McMorrow, *Elements of Modern X-ray Physics*, John Wiley & Sons, Chichester, West Sussex, United Kingdom, 2001.
- 47 S. Stern, *Dissertation*, Universität Hamburg, Hamburg, Germany, 2013.
- 48 R. A. Kirian, X. Wang, U. Weierstall, K. E. Schmidt, J. C. H. Spence, M. Hunter, P. Fromme, T. White, H. N. Chapman and J. Holton, *Opt. Express*, 2010, **18**, 5713–5723.
- 49 D. Waasmaier and A. Kirfel, *Acta Cryst. A*, 1995, **51**, 416–431.
- 50 B. Henke, E. Gullikson and J. Davis, *Atomic Data and Nuclear Data Tables*, 1993, **54**, 181 – 342.
- 51 B. Friedrich and D. Herschbach, *Phys. Rev. Lett.*, 1995, **74**, 4623–4626.
- 52 K. Nakamura, *J. Phys. G*, 2010, **37**, 075021.
- 53 M. Altarelli, R. Brinkmann, M. Chergui, W. Decking, B. Dobson, S. Düsterer, G. Grübel, W. Graeff, H. Graafsma, J. Hajdu, J. Marangos, J. Pflüger, H. Redlin, D. Riley, I. Robinson, J. Rossbach, A. Schwarz, K. Tiedtke, T. Tschentscher, I. Vartanians, H. Wabnitz, H. Weise, R. Wichmann, K. Witte, A. Wolf, M. Wulff and M. Yurkov, *The Technical Design Report of the European XFEL*, Desy technical report, 2007.
- 54 L. Young, E. P. Kanter, B. Kraessig, Y. Li, A. M. March, S. T. Pratt, R. Santra, S. H. Southworth, N. Rohringer, L. F. DiMauro, G. Doumy, C. A. Roedig, N. Berrah, L. Fang, M. Hoener, P. H. Bucksbaum, J. P. Cryan, S. Ghimire, J. M. Glowina, D. A. Reis, J. D. Bozek, C. Bostedt and M. Messerschmidt, *Nature*, 2010, **466**, 56.
- 55 A. Kochur, A. Dudenko, V. Sukhorukov and I. Petrov, *J. Phys. B*, 1994, **27**, 1709.
- 56 M. J. Berger, J. H. Hubbell, S. M. Seltzer, J. Chang, J. S. Coursey, R. Suku-

-
- mar, D. S. Zucker and K. Olsen, *XCOM: Photon Cross Sections Database*, 2010, <http://physics.nist.gov/xcom>, available at <http://physics.nist.gov/xcom>, National Institute of Standards and Technology, Gaithersburg, MD.
- 57 J. L. Hansen, J. J. Omiste Romero, J. H. Nielsen, D. Pentlehner, J. Küpper, R. González-Férez and H. Stapelfeldt, *J. Chem. Phys.*, 2013, **139**, 234313.
- 58 J. Maurer, D. Dimitrovski, L. Christensen, L. B. Madsen and H. Stapelfeldt, *Phys. Rev. Lett.*, 2012, **109**, 123001.
- 59 J. C. Williamson and A. H. Zewail, *Chem. Phys. Lett.*, 1993, **209**, 10 – 16.
- 60 G. Sciaini and R. J. D. Miller, *Rep. Prog. Phys.*, 2011, **74**, 096101.
- 61 Y. Ding, A. Brachmann, F.-J. Decker, D. Dowell, P. Emma, J. Frisch, S. Gilevich, G. Hays, P. Hering, Z. Huang, R. Iverson, H. Loos, A. Miahnahri, H.-D. Nuhn, D. Ratner, J. Turner, J. Welch, W. White and J. Wu, *Phys. Rev. Lett.*, 2009, **102**, 254801.
- 62 Y. Ding, F.-J. Decker, P. Emma, C. Feng, C. Field, J. Frisch, Z. Huang, J. Krzywinski, H. Loos, J. Welch, J. Wu and F. Zhou, *Phys. Rev. Lett.*, 2012, **109**, 254802.
- 63 M. Dohlus, E. A. Schneidmiller and M. V. Yurkov, *Phys. Rev. ST Accel. Beams*, 2011, **14**, 090702.
- 64 R. Weinkauff, P. Schanen, A. Metsala, E. W. Schlag, M. Bürgle and H. Kessler, *J. Phys. Chem.*, 1996, **100**, 18567–18585.
- 65 A. H. Zewail, *J. Phys. Chem. A*, 2000, **104**, 5660–5694.
- 66 J. C. H. Spence, K. Schmidt, J. S. Wu, G. Hembree, U. Weierstall, R. B. Doak and P. Fromme, *Acta Cryst. A*, 2005, **61**, 237–245.
- 67 D. Starodub, R. B. Doak, K. Schmidt, U. Weierstall, J. S. Wu, J. C. H. Spence, M. Howells, M. Marcus, D. Shapiro, A. Barty and H. N. Chapman, *J. Chem. Phys.*, 2005, **123**, 244304.